AIAA JOURNAL
Vol. 46, No. 8, August 2008

Unsteady Wave Phenomena on a Supercritical Airfoil

A. Alshabu* and H. Olivier†
RWTH Aachen University, 52062 Aachen, Germany

DOI: 10.2514/1.35516

Transonic flow investigations are performed in a modified shock tube with a rectangular test section. The investigated model is a BAC3-11 airfoil with a constant cord length and a sharp trailing edge. Time-resolved shadowgraphs and schlieren pictures show pressure waves initiated near the trailing edge and propagating upstream, where they become apparently weaker near the leading edge. These wave processes are accompanied by wake fluctuations and vortex generation in the boundary layer. The observed waves are also captured by pressure transducers mounted in the airfoil model. The dominant frequencies range between approximately 0.7 and 1.5 kHz. Using statistical analysis of the pressure histories, wave propagation direction and wave speed are determined. For higher flow Mach numbers, a strong wave/shock interaction is also observed in which the shock, depending on the shock strength, is attenuated and degenerated into compression waves.

Nomenclature

a_∞	=	sound speed at freestream conditions
c	=	airfoil chord
Ma_s	=	wave Mach number with respect to flow
Ma_∞	=	freestream Mach number
p	=	static pressure
p_t	=	stagnation or pitot pressure
R	=	auto- or cross correlation
Re	=	Reynolds number
T_o	=	stagnation temperature
u	=	velocity
u_{local}	=	local flow velocity
u_w	=	wave speed relative to the airfoil
u^*	=	wave speed relative to the flow
V	=	enclosed volume between pressure sensor and pressure tap
x, y	=	Cartesian coordinates
α	=	angle of attack
γ	=	ratio of specific heats
$\theta_{1,2}$	=	offaxis angles of the optical system
τ	=	time delay

I. Introduction

AN INTERESTING phenomenon is observed when studying transonic flow on an airfoil. Pressure waves build up near the trailing edge and/or in the wake and propagate upstream, where they interact with the incoming flow, strengthen before becoming apparently weaker, and almost disappear near the leading edge. Both experimental and numerical investigations [1] show that the propagation of the observed waves is coupled with vortex generation in the boundary layer and wake fluctuations.

Upstream-moving waves originating at and closely behind the trailing edge in the wake have already been experimentally observed by several authors upon investigating the phenomenon of periodic shock motions on airfoils. These waves are associated with wake fluctuations due to unsteady shock motions and are called "Kutta waves" by Tijdeman [2] (see Fig. 1).

Received 7 November 2007; revision received 4 April 2008; accepted for publication 18 April 2008.

*Research Engineer, Shock Wave Laboratory, Templergraben 55. Member AIAA.

†Professor, Shock Wave Laboratory, Templergraben 55. Member AIAA.

Several explanations of the mechanisms of shock wave oscillation have been advanced by various authors in their investigations using different airfoils and flow conditions. Mundell and Mabey [3] studied the phenomenon of transonic wind-tunnel-wall interference. They suggest that when the shock wave from the airfoil meets the boundary layer on the roof of the wind tunnel, disturbances can propagate upstream along the subsonic portion of the boundary layer and feed back through the freestream to cause shock oscillations. For symmetric airfoils at zero incidence, Gibb [4] postulated that disturbances on one surface of the airfoil will cause an upward deflection of the wake similar to the deflection of a trailing-edge flap. The asymmetric wake causes the shock on the other surface to move toward the rear. The shock waves on the upper and lower surfaces move in antiphase, and the wake is displaced toward the surface on which a shock-induced separation occurs. Antiphase motions of the shock waves are required to generate self-sustained shock oscillations. Stanewsky and Basler [5] performed a wind-tunnel investigation of the buffet characteristics of the CAST 7/DOA1 airfoil. They proposed that the thickening of the boundary layer due to the shock at the trailing edge and the corresponding drop in trailing-edge pressure drive the shock upstream, because the shock strength must adjust according to the trailing-edge pressure. The thickening of the boundary layer at the trailing edge also causes a decambering of the airfoil. This reduces the circulation and results in a decrease in the flow Mach number in the supersonic region and hence the shock strength. Generated pressure disturbances travel upstream along the lower surface, where the flow is accelerated through the pressure drop at the trailing edge. Upon reaching the leading-edge region, these waves cause a change in the stagnation point location. A new flowfield is developed, and the feedback mechanism for unsteady self-sustained shock motion is closed. This mechanism, as explained, is primarily driven by the unsteady boundary-layer behavior.

However, interestingly, we have observed upstream-moving waves for flow conditions for which no shock or shock oscillations occur. Apparently, the vortex generation in the boundary layer and the interaction of vortices with the trailing edge play a key role in the generation of these waves.

In the past, several authors found that a regular Kármán vortex street can also occur in compressible subsonic flows around slender bodies. In the flow pictures presented in their papers, upstream-moving pressure waves could be identified. However, these waves had been thought to be a distortion affecting the vortex street formation and have not been investigated further. Seiler and Srulijes [6] investigated these waves in more detail. They performed experiments on flat plates with different trailing-edge geometries, cylinders, and airfoils. In their work, they reported that the formation of vortices at the trailing edges in compressible subsonic flows is coupled with the emission of upstream-moving pressure waves. However, for airfoils with sharp trailing edges, they could not

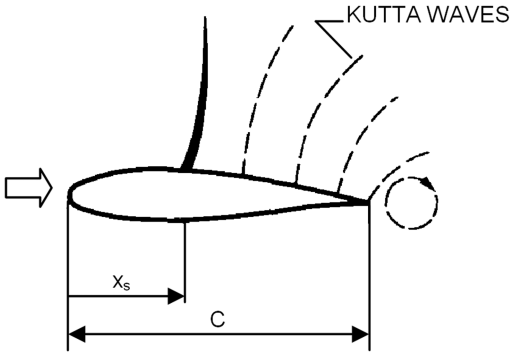

Fig. 1 Propagation of information from the trailing edge to the shock wave [2].

observe the waves. They concluded that the waves represent a weak acoustic phenomenon. Furthermore, they also mentioned the possible influence of these waves on the laminar-turbulent boundary-layer transition.

This paper presents experimental results for better understanding of the preceding wave processes.

II. Experimental Setup

The test facility used is a modified shock tube with a rectangular test section (280×200 mm) to perform airfoil testing at transonic Mach numbers and relatively high Reynolds numbers extending up to 38×10^6 based on a chord length of 100 mm. The flow behind the incident shock wave provides the testing flow for a measurement period of about 5 ms. The facility and its wave plan are depicted in Fig. 2. A full description of the facility and its working principle can be found in [7]. The tested model is a BAC3-11 airfoil with a 200-mm span, 80-mm chord length, and a sharp trailing edge. To perform pressure measurements, 11 pressure transducers are mounted directly beneath pressure taps of 0.6-mm diameter to minimize the influence of the pressure-transmitting volume on the pressure signals (Fig. 3). The enclosed volume V between sensor membrane and pressure tap is 3.45 mm^3. The natural frequency of the Helmholtz resonator [8,9] of the resulting configuration consisting of pressure tap, transmitting volume, and sensor is about 6 kHz. Because of the small thickness of the airfoil model, however, only pressure measurements on one side (in this case, the suction side) are possible, because commercial Kulite XCQ-080 pressure transducers are used. The airfoil model is fixed to the two tunnel side walls by two thin side plates with a thickness of 3 mm. Therefore, either the suction or pressure side of the airfoil and the corresponding flowfield is visible. Because of the high mechanical loading caused by the relatively high stagnation pressure of the flow, the airfoil model cannot be fixed by clamping between the tunnel windows [7]. Figure 4 shows a typical example of a pitot and static pressure history measured in the test section. Because of shock-tube boundary-layer effects, both pressures slightly increase with time. For analyzing data, a time window is chosen between 8 and 12 ms, during which the freestream Mach number changes only by 1.4%. The maximum uncertainty in the measurements is as follows: $p = \pm 3\%$, $Ma = \pm 4.7\%$, $Re = \pm 5.8\%$, and $u = \pm 4.5\%$

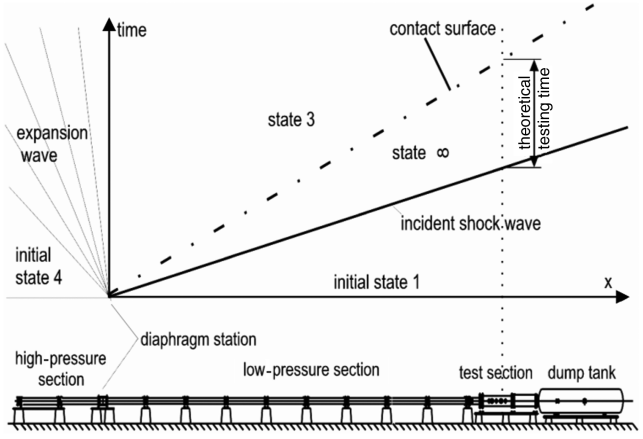

Fig. 2 Transonic shock tube and wave plan.

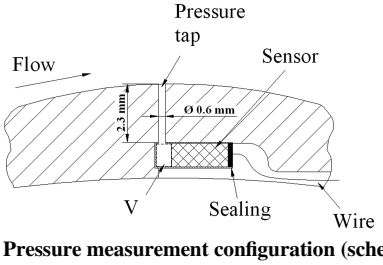

Fig. 3 Pressure measurement configuration (schematic).

For visualizing flow, high-speed photography is used to obtain highly time-resolved shadowgraphs and schlieren pictures of the flow. Figure 5 shows the optical setup that corresponds to the classic Toepler-Z configuration. Shadow and schlieren techniques were applied for visualizing. In both techniques, a flashlight is used as a light source. Two spherical mirrors of a focal length of 2000 mm generate parallel light beams crossing the test section. A focusing lens creates an image of the shadow plane on the camera film. For the schlieren technique, a circular filter mask is placed close to the focal plane of the first spherical mirror. An iris diaphragm serves as a cutoff device in the focal plane of the second spherical mirror. A cylindrical lens is used to minimize the astigmatism error. Moreover, aberration errors introduced by the spherical mirrors are minimized by keeping the offaxis angles small ($\theta_{1,2} \approx 6.9$ deg). The applied camera is a high-speed Shimadzu HPV-1 digital camera. This camera can capture up to 1 million frames per second with a maximum of 100 frames. A constant spatial resolution of 312×260 pixels is maintained at all recording speeds. Frames presented in this paper were obtained at a frequency of 125 kHz with a chip exposure time of 1 μs.

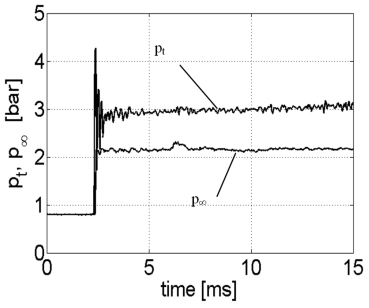

Fig. 4 Pitot and static pressure histories measured in the test section of the transonic shock tube.

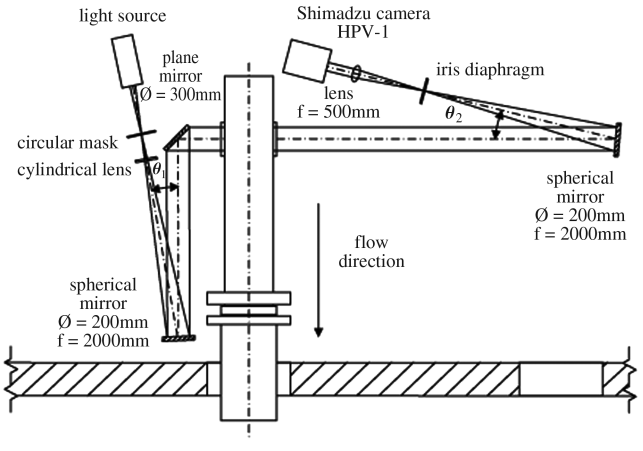

Fig. 5 Schematic sketch of optical setup.

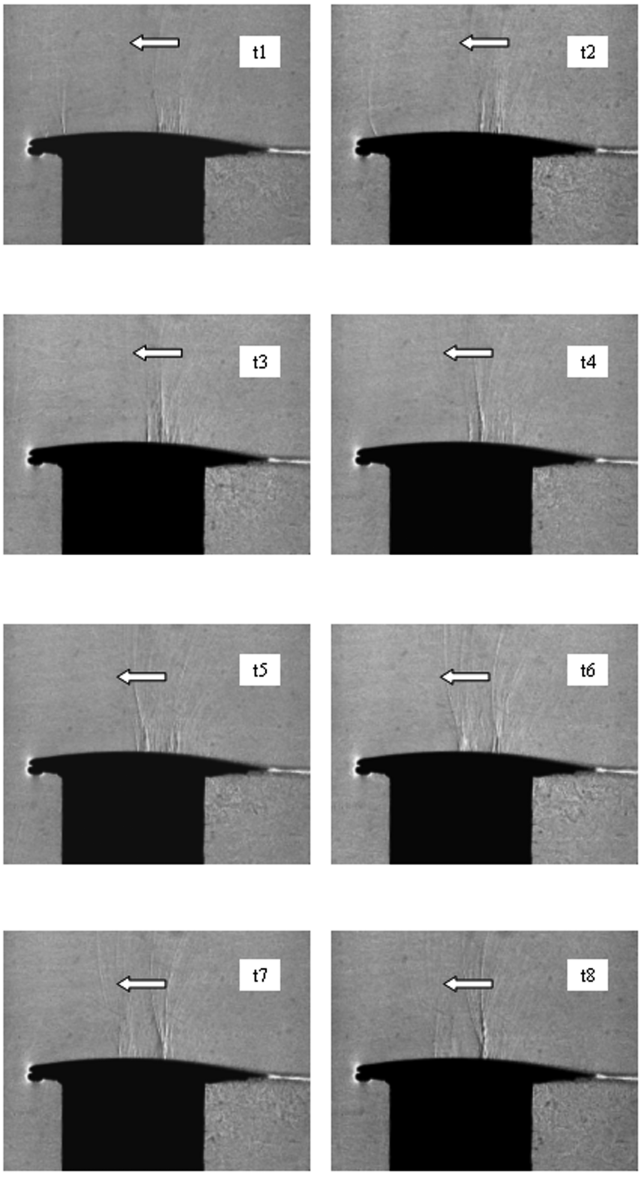

Fig. 6 Time-resolved shadowgraphs showing the wave propagation on the suction side of the airfoil BAC3-11; $Ma_\infty = 0.72$, $Re = 2.0 \times 10^6$, $\alpha = 0$ deg, and $\Delta t = 0.1$ ms.

III. Results

The experiments are conducted at chord Reynolds numbers ranging from 1.0 to 4×10^6. The Mach numbers are between 0.65 and 0.8 at zero incidence. The corresponding stagnation pressure and temperature ranges are 1.7 to 7.5 bar and 428 to 492 K, respectively. Figure 6 shows time-resolved shadowgraphs for an experiment with a Mach number of 0.72 and a Reynolds number of 2.0×10^6. The wave structure on the suction side of the airfoil and the upstream propagation of the waves can be easily seen. An increase in the wave intensity is also seen in the region of maximum thickness of the airfoil. The intensity of the waves decreases, however, as they move further upstream toward the leading edge. Here, they become almost invisible, depending on the sensitivity of the shadowgraph system. Because of the line-of-sight effect of the shadowgraphs and the limited sensitivity of the optical system, it is difficult to identify vortex structures in the shadowgraphs. However, numerical simulations [10] confirm that the wave generation is coupled with vortex generation in the boundary layer (Fig. 7). These vortices propagate downstream and interact with the trailing edge and/or the wake, causing the waves to initiate. This shows that the vortex generation in the boundary layer seems to play an important role in the wave generation. Consequently, we suppose that to control the wave generation, both the vortex generation and the interaction of the vortices with the trailing edge have to be influenced.

Parallel to flow visualizations, pressure measurements on the suction side of the BAC3-11 airfoil were also performed. Figure 8 shows some selected pressure histories for an experiment with a Mach number of 0.71 and a Reynolds number of 2.0×10^6. Pressure fluctuations in the pressure histories resulting from the aforementioned wave processes can be seen. Starting from the trailing edge, the intensity of these fluctuations increases in the region of maximum thickness of the airfoil before decreasing strongly near the leading edge. This confirms the conclusion made from the shadowgraphs. As described next, these fluctuations were analyzed by statistical means.

Figure 9 shows the standard deviation of the obtained pressure signals for the time interval from 8 to 12 ms, normalized with the freestream static pressure p_∞. The standard deviation, which can be regarded as a measure of the wave intensity, confirms the preceding conclusion. Starting with pressure fluctuations of about 2.5% at the chord position $x/c = 0.73$, the pressure fluctuations intensify upstream, reaching a maximum of about 3.5% at $x/c = 0.49$ before decreasing rapidly further upstream to less than 1.0% at $x/c = 0.18$. In Fig. 10, the autocorrelation functions for the pressure histories at the positions $x/c = 0.37$ and 0.73 are shown. The repeated peaks of the autocorrelation functions indicate the periodical nature of the

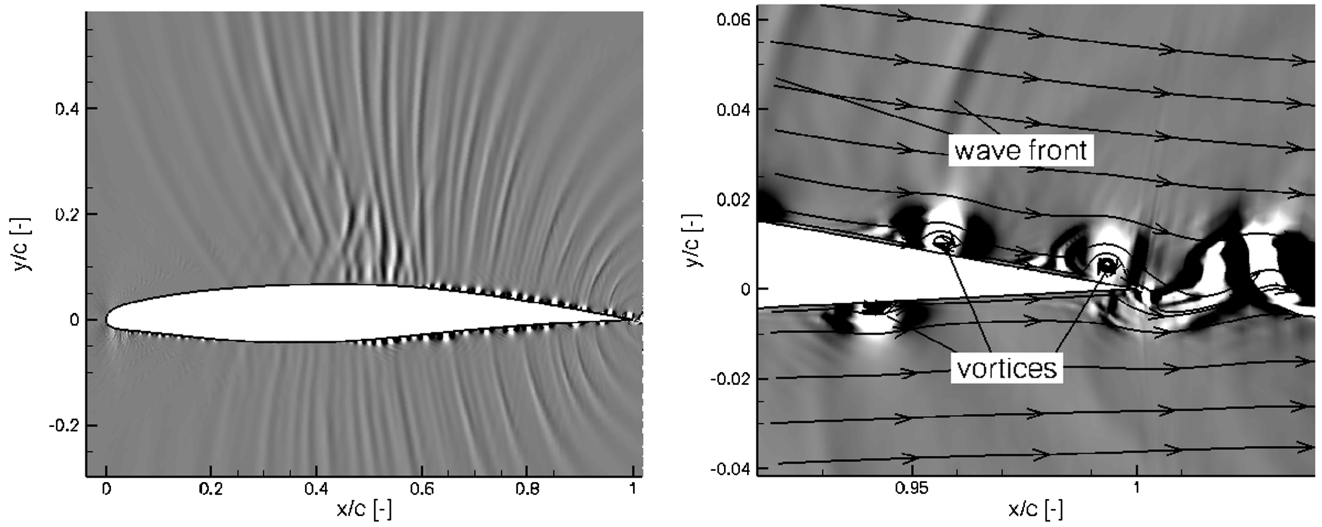

Fig. 7 Numerical results [10]: wave structure on the suction side of BAC3-11 airfoil (left) and vortex interaction at the trailing edge (right); $Ma_\infty = 0.71$, $Re = 3.1 \times 10^6$, and $\alpha = 0$ deg.

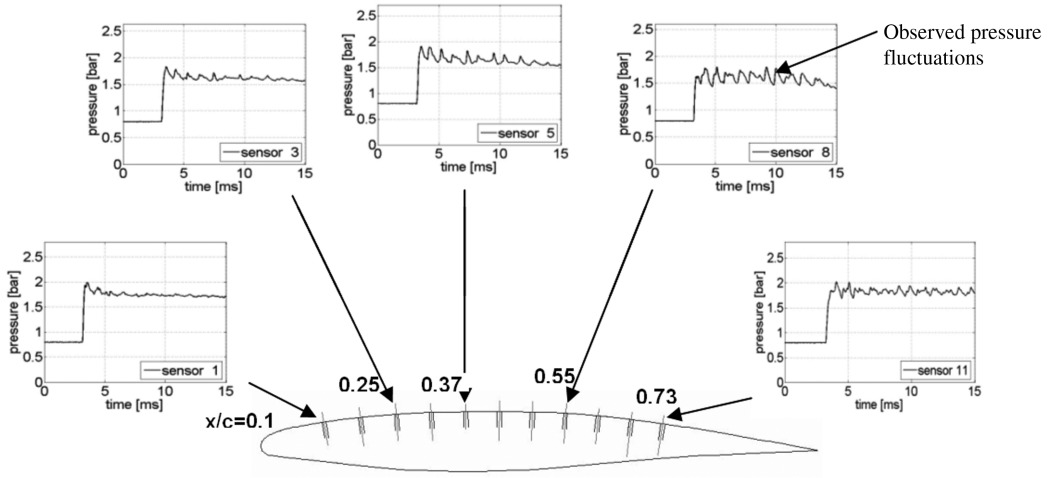

Fig. 8 Pressure histories along the suction surface of the BAC3-11 airfoil; $M\infty = 0.71$, $Re = 2.0 \times 10^6$, and $\alpha = 0$ deg.

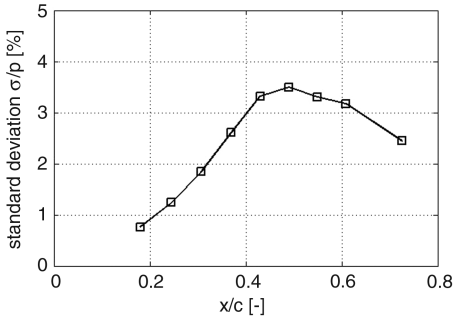

Fig. 9 Standard deviation of the pressure histories normalized with p_∞; time period from 8 to 12 ms; $Ma_\infty = 0.71$, $Re = 2.0 \times 10^6$, and $\alpha = 0$ deg.

wave processes, and the two neighboring peaks indicate the existence of two predominant frequencies represented in the signal. Figure 11 shows a Fourier analysis (power spectral density) of the same pressure histories presented in Fig. 10. Figure 11 reveals two predominant frequencies ranging from 0.7 to 1.5 kHz, as concluded from the autocorrelation function. The same holds for other pressure histories.

Two-point cross correlation of the pressure histories was applied to determine the propagation direction and speed of the observed waves. For each pressure history, the cross-correlation function was calculated with all other pressure histories. By using the cross correlation, the time required for one wave to travel between two pressure sensors could be determined. The averaged wave speed between the sensors could be estimated by knowing the distance between the sensors. The wave speed could not be determined between $x/c = 0.11$ and 0.25, because in this region, the correlation was too weak for reliably calculating the wave speed. Furthermore, sensor 10 at the position $x/c = 0.67$ exhibited a longer rise time than with the other sensors, and thus it was not considered in the wave speed calculations. Figure 12 shows the cross correlation of the two pressure tap positions considered in Fig. 10 and the estimated wave speed at the corresponding position. The negative time delays of the correlation function of the pressure sensors located upstream of the considered position 11 indicate that the pressure waves propagate upstream Fig. 12 (right). Depending on the relative position of the two sensors being correlated, positive or negative time delays result, as shown in Fig. 12 (left). Except at the chord positions $x/c = 0.31$ (fourth position in Fig. 8) and 0.73, the estimated wave speed at each sensor position is calculated as an average of the wave speeds of the next two neighboring sensors. At the positions $x/c = 0.31$ and 0.73, the wave speed is simply the estimated speed between the considered and the next neighboring sensor. To determine the wave speed with respect to flow, the local flow velocity has to be added. Figure 13 shows the wave speed relative to the airfoil. Regardless of the rough spatial resolution, the figure displays the expected behavior of the wave speed. It can be easily seen that the wave speed is lowest in the region of high local flow velocities and increases further downstream in the recompression zone of the airfoil.

One can compare the wave Mach number with respect to flow given by Eq. (1) with the wave speed estimated by the cross correlation. For the pressure amplitudes seen in Fig. 14, a typical wave Mach number of about $Ma_s = 1.02$ to 1.04 results, whereby $p21 = p_2/p_1 \approx 1.05$ to 1.1, $\gamma = 1.4$, and

$$Ma_s = \sqrt{\frac{(\gamma+1)p_{21} + \gamma - 1}{2\gamma}} \tag{1}$$

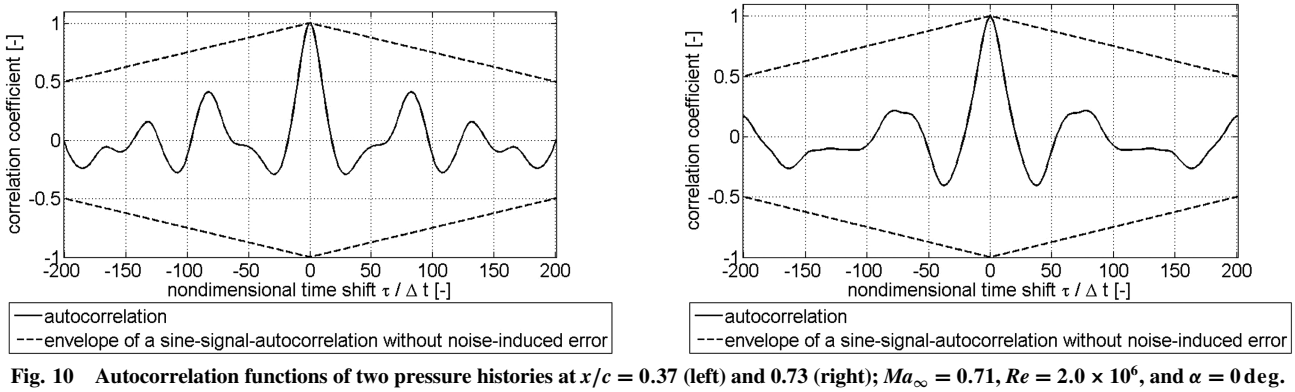

Fig. 10 Autocorrelation functions of two pressure histories at $x/c = 0.37$ (left) and 0.73 (right); $Ma_\infty = 0.71$, $Re = 2.0 \times 10^6$, and $\alpha = 0$ deg.

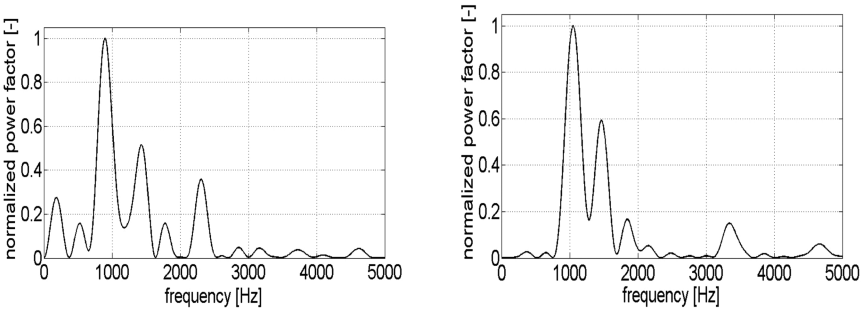

Fig. 11 Power spectral densities of two pressure histories at $x/c = 0.37$ (left) and 0.73 (right); $Ma_\infty = 0.71$, $Re = 2.0 \times 10^6$, and $\alpha = 0$ deg.

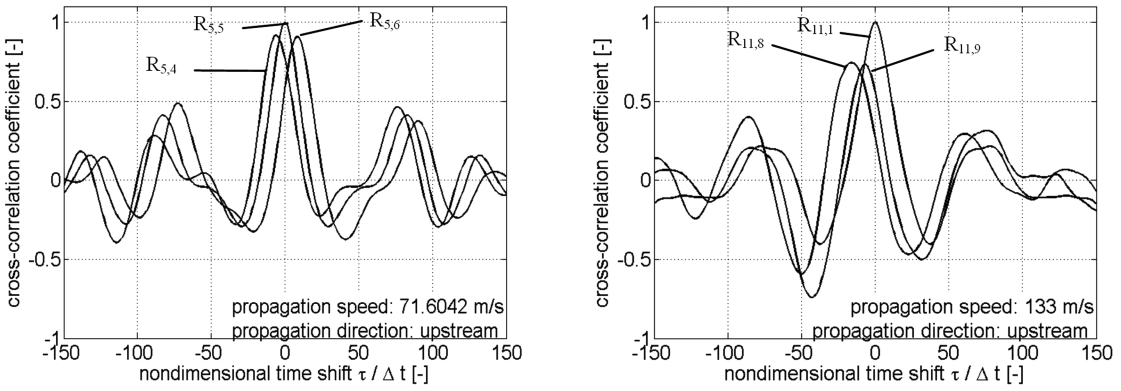

Fig. 12 Cross-correlation functions of two pressure sensor signals at $x/c = 0.37$ (left) and 0.73 (right) with some selected pressure gauges located up- and downstream of the considered position; $Ma_\infty = 0.71$, $Re = 2.0 \times 10^6$, and $\alpha = 0$ deg.

The absolute wave speed for the given example can be estimated as follows. The wave speed with respect to the local flow is approximated by

$$u^* = u_w + u_{\text{local}} \approx u_w + Ma_\infty \cdot a_\infty$$

Considering a wave velocity of $u_w = 133$ m/s, which occurs at the rear part of the airfoil (see Fig. 13), a freestream Mach number of $Ma_\infty = 0.71$ and a freestream sound speed of $a_\infty = 410$ m/s, a wave speed of $u^* = 424$ m/s results and, therewith, a wave Mach number of $Ma_s = u^*/a_\infty = 1.03$.

Both results (namely, the wave Mach number deduced from the measured pressure amplitudes and from the determined wave velocities) are in good agreement. For the preceding estimation, the wave speed at the chord position $x/c = 0.73$ was chosen, because the difference between the local and the freestream flow speeds is smallest at this sensor position. One should note here that the preceding simple comparison applies only if the local flow velocity can be approximated quite well by the freestream velocity. However, this comparison reveals the usefulness of computing the wave speeds by statistical analysis. Furthermore, the obtained wave Mach numbers show that, as expected, the waves relative to the flow propagate slightly faster than the speed of sound.

A. Influence of the Mach and Reynolds Numbers

In this section, some results regarding the influence of the Mach and Reynolds number on the wave characteristics are discussed. Figure 15 shows three shadowgraphs of the flow on the suction side of the airfoil at different flow conditions. As depicted in Figs. 15a and 15b, an increase in the Mach number leads to an increased wave intensity. In addition, the complexity of the wave structure increases for higher Mach numbers. This is caused by the interaction of the waves with some stronger local supersonic regions established at higher Mach numbers. At higher Reynolds numbers, the wave structure becomes more complex too (Fig. 15c). However, because of the increased sensitivity of the optical system at higher Reynolds numbers resulting from higher densities, it is not easy to judge the dependence of the wave intensity on the Reynolds number via shadowgraphs.

Figures 16a and 16b demonstrate the influence of the Mach number on the wave intensity and wave speed, respectively. As seen in Figs. 16a and 16b, higher Mach numbers result in larger wave

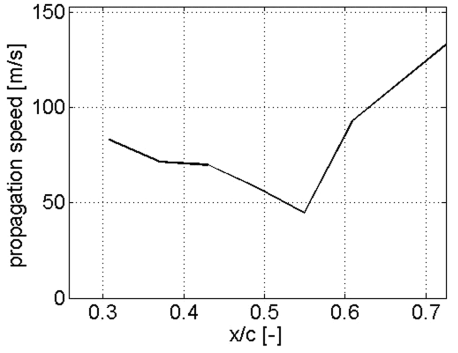

Fig. 13 Determined wave speed along BAC3-11 airfoil suction side; $Ma_\infty = 0.71$, $Re = 2.0 \times 10^6$, and $\alpha = 0$ deg.

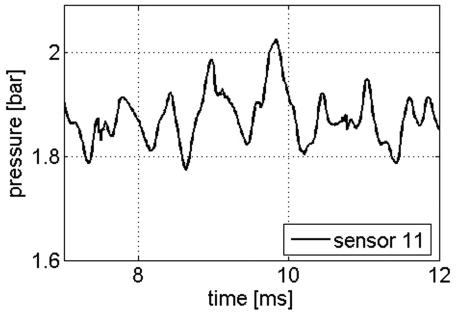

Fig. 14 Part of the pressure history; $x/c = 0.73$, $Ma_\infty = 0.71$, $Re = 2.0 \times 10^6$, and $\alpha = 0$ deg.

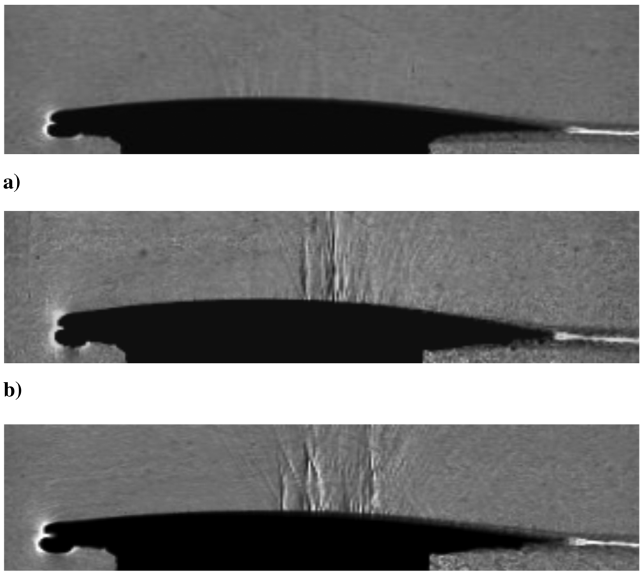

a)

b)

c)

Fig. 15 Influence of the Mach and Reynolds numbers on the wave structure: a) $Ma_\infty = 0.67$ and $Re = 2.0 \times 10^6$, b) $Ma_\infty = 0.72$ and $Re = 2.0 \times 10^6$, and c) $Ma_\infty = 0.72$ and $Re = 3.0 \times 10^6$.

intensities and an overall decreased wave speed with respect to the airfoil. In Fig. 17a, it might be deduced that a small increase in the Reynolds number of about 1×10^6 results in a small increase in the wave intensity. The influence of the Reynolds number on the wave intensity does not seem to be as strong as that of the Mach number. Furthermore, for the considered Reynolds number range, the Reynolds number does not significantly influence the wave speed, as it is depicted in Fig. 17b. The small deviation in the wave speeds shown in Fig. 17b might be explained by the small deviation in the Mach number.

B. Wave/Shock Interaction

For higher flow Mach numbers, the supersonic region on the suction side of the airfoil is terminated by shocks, as shown in Figs. 18 and 19. Figure 18 presents two shadowgraphs of an experiment for a Mach number of 0.76 and a Reynolds number of 1.0×10^6. In Fig. 18a, a lambda shock, typical for a laminar shock/boundary-layer interaction, can be seen. Time-resolved shadowgraphs of this experiment show a strong wave/shock interaction in which the shock for short periods of time is altered and degenerated into compression waves, as depicted in Fig. 18b. It might be interesting to further investigate this phenomenon to find out whether it can be controlled and used to attenuate the shock and thus reduce the wave drag. The first numerical simulations performed for a simple wave/shock interaction model indicate that the time-averaged shock intensity can be reduced by the wave interaction.

Figure 19 shows a schlieren picture for an experiment with a Mach number of 0.80 and a Reynolds number of 3.4×10^6. Here, a large supersonic region visible by a field of Mach lines and terminated by a cambered shock can be clearly seen. At this Reynolds number, the boundary layer upstream of the shock is turbulent so that no lambda shock forms. The strong shock causes a significant flow separation, as seen in Fig. 19. A dark region is also observed immediately downstream at the midheight of the shock. A corresponding colored schlieren picture (not shown in this paper) indicates that this region represents an expansion region. The expansion region might be formed by the observed strong wave/shock interaction or, more likely, by the shock shape itself. Because of the cambering of the shock, the shock part ahead of the dark region can be considered as a normal shock with the highest pressure jump. To adjust this high-

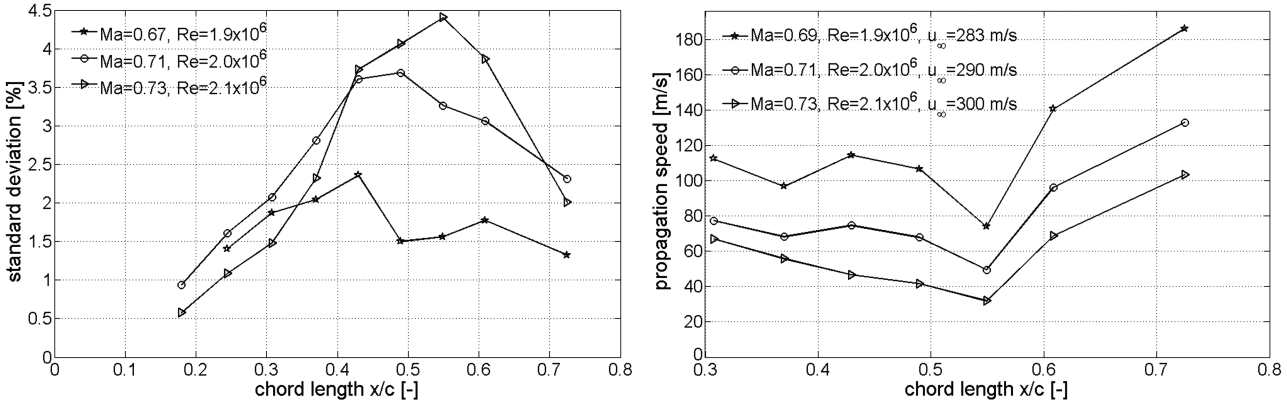

a) b)

Fig. 16 Mach number dependence of wave intensity (left) and wave speed (right).

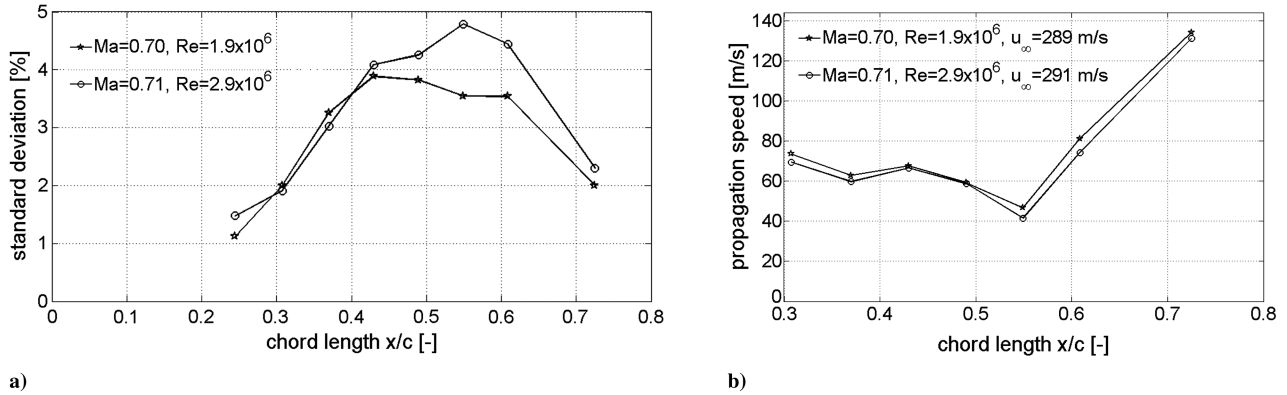

a) b)

Fig. 17 Reynolds number dependence of wave intensity (left) and wave speed (right).

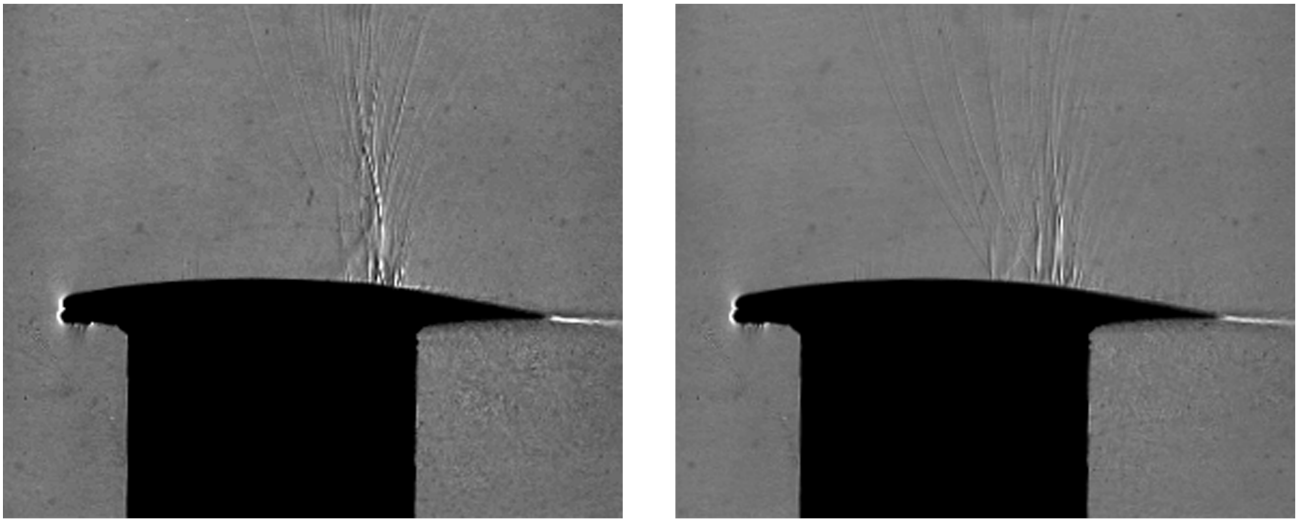

a) b)

Fig. 18 Time-resolved shadowgraph showing wave/shock interaction; $Ma_\infty = 0.76$ and $Re = 1.0 \times 10^6$; time delay between the pictures is 0.26 ms.

pressure region to the lower-pressure regions adjacent to the normal shock part, the flow has to expand in this region. Moreover, one notices that the upstream propagation of the waves is hindered by the shock. The waves can only propagate around the shock in the subsonic flowfield. At the sonic line separating the subsonic flowfield from the supersonic flowfield, the waves generate weak pseudo-upstream-moving waves in the supersonic region, as depicted in Fig. 20. In the supersonic part of the flowfield, the wave-induced disturbances are certainly traveling downstream with respect to flow. Finally, no significant Mach and Reynolds numbers dependence of the wave frequencies was found in the investigated range of flow conditions.

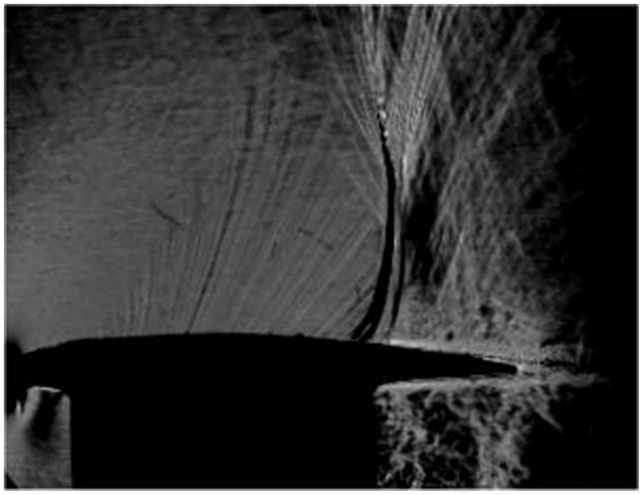

Fig. 19 Schlieren picture showing a wave/shock interaction; $Ma_\infty = 0.80$, $Re = 3.4 \times 10^6$, and $\alpha = 0$ deg.

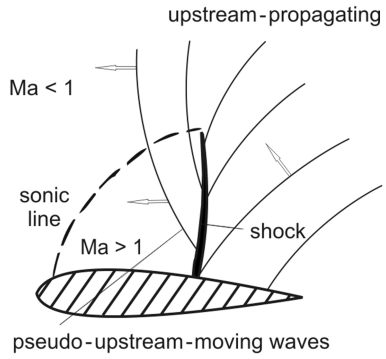

Fig. 20 Schematic drawing of wave propagation in the sub- and supersonic flow regions.

IV. Conclusions

Time-resolved shadowgraphs and schlieren pictures clearly reveal the existence of upstream-moving waves. These waves start near the trailing edge and/or in the wake and propagate upstream. Approaching the leading edge, the waves become apparently weaker and almost disappear. For higher Mach numbers, large supersonic regions terminated by shocks hinder the direct upstream propagation of the waves. In this case, the waves pass around the shock in the subsonic part of the flowfield. Depending on the shock strength, a strong wave/shock interaction can be observed in which the shock is attenuated and degenerated into compression waves. The wave generation is coupled with vortex generation in the boundary layer. These vortices propagate downstream and interact with the trailing edge and the wake, causing the waves to initiate. Small supersonic pockets located on the top of each vortex seem to be responsible for the wave generation. Thus, the vortex generation in the boundary layer plays a major role in the wave generation process. Time-resolved pressure measurements show pressure fluctuations caused by the preceding wave processes. For the considered flow conditions, Fourier analysis of the pressure histories reveals two predominant frequencies in the range between 0.7 and 1.5 kHz. Using two-point cross correlation, the wave speed and wave propagation direction are determined. As expected, the wave Mach number is just above 1, which shows that with respect to flow, the waves propagate slightly faster than the speed of sound. Within the investigated range of flow conditions, the wave intensity primarily depends on the Mach number and is less dependent on the Reynolds number. Moreover, the determined wave speed relative to the airfoil model increases with increasing Mach number and exhibits no significant Reynolds number dependence. Finally, the obtained wave frequencies show no Mach and Reynolds numbers dependence in the investigated range of flow conditions. The preceding wave processes are very interesting for the aerodynamics of airfoils. First, these waves could influence the laminar-turbulent transition in the boundary layer, because they represent pressure gradients traveling toward the leading edge. Second, the observed wave/shock interaction in which the shock attenuates and degenerates into compression waves might open new possibilities for reducing wave drag.

Acknowledgments

This work was funded by the German research association Deutsche Forschungsgemeinschaft as a part of the research collaboration Sonderforschungsbereich 401 "Flow Modulation and Fluid-Structure Interaction at Airplane Wings" at the RWTH Aachen University. The authors would like to thank H. Kleine from the University of New South Wales for fruitful discussions and assistance setting up the optical system and performing the flow visualization. Furthermore, we would like to thank K. Tsuji from the Shimadzu Corporation for providing the high-speed camera HPV-1 for the experiments.

References

[1] Alshabu, A., Olivier, H., and Klioutchnikov, I., "Investigation of Upstream Moving Pressure Waves on a Supercritical Airfoil," *Aerospace Science and Technology*, Vol. 10, May 2006, pp. 465–473. doi:10.1016/j.ast.2006.04.003

[2] Tijdeman, H., "Investigation of the Transonic Flow Around Oscillating Airfoils," National Aerospace Lab. NLR TR-77090, Amsterdam, Oct. 1977.

[3] Mundell, A. R. G., and Mabey, D. G., "Pressure Fluctuations Caused by Transonic Shock/Boundary Layer Interaction," *The Aeronautical Journal*, Vol. 90, Aug.–Sept. 1986, pp. 274–281.

[4] Gibb, J., "The Cause and Cure of Periodic Flows at Transonic Speeds," *16th Congress of the International Council of Aeronautical Science*, AIAA, Washington, D.C., Aug.–Sept. 1988, pp. 1522–1530.

[5] Stanewsky, E., and Basler, D., "Experimental Investigation of Buffet Onset and Penetration on a Supercritical Airfoil at Transonic Speeds," *Aircraft Dynamic Loads Due to Flow Separation*, AGARD CP-483, AGARD, Neuilly-sur-Seine, France, Sept. 1990, pp. 4.1–4.11.

[6] Seiler, F., and Srulijes, J., "Vortices and Pressure Waves at Trailing Edges," *Proceedings of the 16th International Congress on High Speed Photography and Photonics*, Strasbourg, France, 1984.

[7] Olivier, H., Reichel, T., and Zechner, M., "Airfoil Flow Visualization and Pressure Measurements in High-Reynolds-Number Transonic Flow," *AIAA Journal*, Vol. 41, No. 8, Aug. 2003, pp. 1405–1412.

[8] Göpel, W., Hesse, J., and Zemel, J. N. (eds.), *Sensors: A Comprehensive Survey*, Vol. 7, Wiley, New York, 1994.

[9] Gossweiler, C., "Sonden und Messsystem für Schnelle Aerodynamische Strömungsmessung mit Piezoresistiven Druckgebern," Ph.D. Dissertation, ETH Zürich, Zürich, 1993.

[10] Klioutchnikov, I., and Ballmann, J., "DNS of Transitional Transonic Flow About a Supercritical BAC3-11 Airfoil Using High-Order Shock Capturing Schemes," *Direct and Large-Eddy Simulation VI*, ERCOFTAC Series, Vol. 10, Springer–Verlag, Dordrecht, The Netherlands, 2006, pp. 737–744.

N. Chokani
Associate Editor